Article

Modeling adhesive hysteresis

Anle Wang [1], Yunong Zhou [1] and Martin H. Müser [1,*]

[1] Department of Material Science and Engineering, Saarland University, Campus C6 3, 66123, Saarbrücken, Germany

* Correspondence: martin.mueser@mx.uni-saarland.de

Version August 7, 2020 submitted to Lubricants

Abstract: When an elastomer approaches to or retracts from an adhesive indenter, the elastomer's surface can suddenly become unstable and reshape itself quasi-discontinuously, e.g., when small-scale asperities jump into or snap out of contact. Such dynamics induce a displacement hysteresis between approach and retraction. In this study, we quantify the ensuing unavoidable energy loss for rigid indenters with surface flat and Hertzian surface profiles using analytical and numerical methods. The range of adhesion turns out to be central in particular during the rarely modeled approach-to and subsequent jump-into contact. Central attention is paid to the design of cohesive-zone models allowing dynamical processes in the absence of high symmetries to be efficiently simulated. Our study includes a Griffith's type analysis for the energy lost during fracture and regeneration of a flat interface. It reveals that the leading-order corrections of the energy loss being due to finite-range adhesion only disappear with the third root of the linear mesh size, while leading-order errors in the pull-off force disappear linearly.

Keywords: adhesion; cohesive zone model; hysteresis

1. Introduction

Adhesion between solid bodies plays an important role in nature and technology. Usually, it is strongly suppressed due to the presence of roughness, which exists even for highly polished surfaces [1]. However, when one of the two solid bodies is very compliant, adhesion can become noticeable at relatively large scales and be exploited technologically [2].

The optimization of adhesive structures can certainly benefit from modeling adhesion, which, however, is not always a trivial task. One difficulty is that adhesion tends to be very short ranged, which leads to stiff differential equations to be solved when describing a structure at a coarse scale. A popular method to avoid singularities and to reduce the stiffness of adhesive contact problem is to use so-called cohesive-zone models (CZMs) [3–5]. They describe, usually in analytical form, how the traction depends on the local separation between two surfaces. CZMs are commonly stated and used for a given pair of surfaces irrespective of the scale to which the surface is discretized.

Traditionally CZMs [6] are constructed in a top-down fashion, i.e., surface energy γ and Tabor parameter μ_{T}, a measure for the range of adhesion, are determined at an intermediate length scale, and the parameters of a given CZM are adjusted such that these two target numbers are reproduced. It was shown for adhesive Hertzian contacts that details of the functional form of CZM's do not significantly affect how contact area and displacement change as a function of normal load as long as γ and μ_{T} are matched [7].

So far, there have been only few attempts [8,9] to construct CZMs from the bottom up. However, it appears to be generally accepted that they are best given by the interaction energy per surface area that two solid bodies with atomically flat surfaces would have as a function of their distance [3]. Using CZMs that reflect the microscopic short range of adhesion realistically either requires a very

fine discretization or induces unrealistic force-displacement dependencies [10]. When the grid is not sufficiently fine, jump-in or snap-out dynamics usually suffer from unacceptably large errors, e.g., the pull-off force and work of separation can be largely overestimated [11]. A frequent solution to this problem is a mesh refinement in the zone of interest, which, however, implies a low computational efficiency. Unfortunately, there does not appear to be a generally accepted, or well tested rule for how to best select the mesh. When it cannot be made very fine, the most common way to proceed is to reduce the surface energy, whereby realistic traction forces [3,12–17] can be obtained. However, it is unclear if this is the best course of action, or, if it could sometimes be better to change the range of interaction instead.

In this work, we propose a rule for how to select the mesh size for a given CZM, and more importantly, we provide a recipe for how to redesign it such that it provides accurate force-displacement dependencies if the mesh size cannot be made arbitrarily small. Towards this end we focus on the case of a smooth flat elastomer in contact with a rigid, flat, smooth indenter with adhesive interaction as the most basic model and explore the following two questions: At what point is a mesh size inadequate? How can a CZM be redefined at a coarse scale such that the work of separation and the energy hysteresis that in a closed compression-decompression loop are similar to their results obtained in a refined calculation using the "exact" CZM?

Another issue has been discussed surprisingly little, namely, whether a given CZM reproduces a realistic approach curve. One of us found that a Tabor parameter of $\mu_{\mathrm{T}} = 4$ produces a load-displacement curve similar to the well-known limit proposed by Johnson, Kendall, and Robertson (JKR) [18], while the approach remained – as almost always – unexplored. The latter, however, is decisive for the unavoidable energy loss that ensues as a consequence of the difference between the approach and the retraction curve. In fact, a Tabor parameter of $\mu_{\mathrm{T}} = 4$ leads to a negligible hysteresis as is demonstrated in this study. Since it is concerned with hysteresis, we also scrutinize the seemingly boring approach curve and discuss why we are critical of common ways to model approach.

The reminder of this paper is organized as follows: The model and the computational method are presented in Sect. 2. Sect. 3 contains analytical and numerical approaches to the contact between two adhesive, originally flat adhesive surfaces, including a guideline for the construction of scale-dependent CZMs. This guideline is then applied in Sect. 4 to an uneven surface, namely to a smooth Hertzian indenter. Conclusions are drawn in the final Sect. 5.

2. Model and method

2.1. Model

We consider an adhesive, flat, linearly elastic, semi-infinite elastomer interacting with a rigid indenter. The center-of-mass of the elastomer's bottom surface, u_0, is gradually decreased from a large positive value, clearly exceeding the characteristic length of attraction, to a value, where elastomer and indenter repel each other and then increased again back to its original value. The internal degrees of freedom, as denoted by $u(\mathbf{r})$ in real space or by its Fourier transform $\tilde{u}(\mathbf{q})$, are allowed to take arbitrary values except for the center-of-mass mode $u_0 = \tilde{u}(0)$, see Fig. 1. The elastic energy to deform the (surface of the) elastomer is given by

$$V_{\mathrm{ela}} = A \sum_{\mathbf{q}} \frac{qE^*}{4} |\tilde{u}(\mathbf{q})|^2, \tag{1}$$

where E^* is the elastomer's contact modulus and q is the magnitude of $\mathbf{q} = (q_x, q_y)$. The square domain has an area of $A = L^2$, where L is the system's linear dimension. The central image is repeated periodically in x and y direction,

The default geometry of the rigid indenter is flat, however, uneven surfaces are considered as well. The xy-plane is located such that it cuts through the indenter's highest point. The contact between

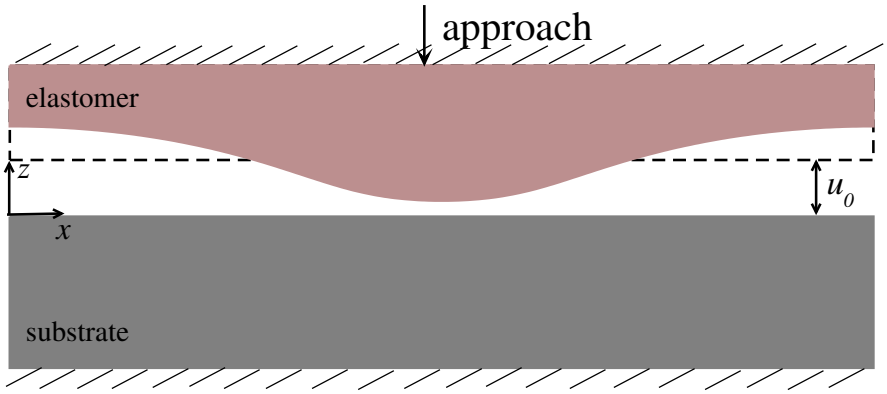

Figure 1. Schematic illustration of the computational model. The elastomer is moved relative to a rigid indenter such that the center-of-mass position of the elastomer's lower surface is constrained to a (time-dependent) value. The remaining internal degrees of freedom are allowed to relax to a configuration minimizing the total (potential) energy.

elastomer and indenter is frictionless. Furthermore, the interfacial energy per simulation cell is defined as

$$V_{\text{int}} = \int_A d^2r\, \gamma(\mathrm{r}) \tag{2}$$

with the interfacial energy density given by, for example, a relation inspired by the Morse potential

$$\gamma_{\text{M}}(\mathbf{r}) = \gamma \left[e^{-2\{g(\mathbf{r})-\rho_0\}/\rho} - 2\, e^{-\{g(\mathbf{r})-\rho_0\}/\rho} \right], \tag{3}$$

where γ is the (maximum) surface energy, ρ the decay length of the adhesion, and ρ_0 the equilibrium separation between indenter and elastomer. The latter is set to $\rho_0 = 0$, since it constitutes only an offset, which can be deemed irrelevant in a continuum treatment. The function $g(\mathbf{r}) = u(\mathbf{r}) - h(\mathbf{r})$ indicates the gap or interfacial separation between elastomer and indenter as a function of the in-plane coordinate $\mathbf{r} = (x, y)$, where $h(\mathbf{r})$ states the shape of the indenter. For a flat indenter, $h(\mathbf{r}) \equiv 0$.

The original rationale for the choice of this particular interaction law, which is also known as Morse potential, was as follows: An exponential attraction as cohesive zone model was reported to yield smooth responses [19,20]. For reasons that should become obvious later in this work, we want the interaction to be at least twice differentiable so that a hard-wall repulsion is no option. The Morse potential is then beneficial, because the repulsive stress can be computed by squaring the exponential function $\exp\{-g(\mathbf{r})/\rho\}$ without having to evaluate another exponential. Moreover, the curvature in the energy minimum is relatively modest (which is beneficial for simulations). Finally, it is relatively easy to change the interaction range by replacing ρ with a different value, without having to reparametrize the prefactor γ.

Alternatively, it would have been possible to use, for example, a $m - n$ Mie potential,

$$\gamma_{\text{Mie}}(g) = \gamma\, \frac{m\, n}{m - n} \left\{ \frac{1}{m} \left(\frac{g}{\rho} \right)^{-m} - \frac{1}{n} \left(\frac{g}{\rho} \right)^{-n} \right\}$$

with $m > n > 0$ being real numbers. The Mie potential is sometimes misleadingly said to be a generalization of Lennard-Jones, however, Mie [21] introduced his potential more than two decades before Lennard-Jones [22]. An effective $8 - 2$ Mie potential between surface points ensues from Lennard-Jones interactions between two semi-infinite bodies within the Derjaguin approximation [23].

Since both considered potentials have the property that repulsion decreases more quickly with distance than attraction, they should lead to qualitatively similar behavior, just like other potentials with that property. However, moderate changes in the adhesion law can still affect some computed

properties quite substantially. This is why some thought should be spent on the choice of the potential. If the goal is to construct a CZM starting from the atomic scale, a properly constructed Mie potential would be a good candidate, in particular if the adhesion arises mainly from dispersive or van-der-Waals forces. If, however, the mesh-elements are more than a few microns in size, the CZM should reflect the proper contact mechanics of the underlying microscopic (random) roughness and the functional form be chosen accordingly. As we find in preliminary simulations of adhesive, randomly rough surfaces, these CZMs can be similar to the Morse potential, as they can be well described by a difference between two exponentially decaying functions. In fact, a purely repulsive, non-overlap constraint between an elastomer and a randomly rough surface effectively leads to an exponential between the two surfaces [24,25]. If, however, the goal is to reach the continuum limit as quickly as possible, yet different choices are possible, e.g., the one introduced later in Eq. (31).

For the simulations on ideally flat surfaces in this study, we decided to use the Morse potential. In hindsight, we could argue that this was done to represent the formation and the detachment of a randomly rough surfaces at a coarse scale. Two properties of the Morse surface-energy density are needed in the remainder of this article. First, the maximum tensile traction, i.e., the maximum of the first derivative of the r.h.s. of Eq. (3). It is given by $\sigma_{\max} = \gamma/(2\rho)$ and located at an interfacial separation of $g = \rho \ln 2$. Second, the negative minimum curvature, which can be deduced to be $\kappa_{\max} = \gamma/(4\rho^2)$. It occurs at an interfacial separation of $g = \rho \ln 4$. Also note that the radius of curvature of a flat contact is formally infinite (at least in the limit $L \to \infty$) so that the (usual) Tabor parameter can be said to diverge automatically and thus the interaction to be short ranged irrespective of the numerical value of ρ.

2.2. Method

The system is displacement-driven rather than force-driven, i.e., depending on the mean gap u_0 between elastomer and indenter, the total potential energy

$$V_{\text{tot}}[g_0, u(\mathbf{r})] = V_{\text{ela}}[u(\mathbf{r})] + V_{\text{int}}[g_0, u(\mathbf{r})] \tag{4}$$

is minimized by a structured or unstructured displacement field $u(\mathbf{r})$. Minimization is done using Green's function molecular dynamics (GFMD) [26], in which the elastomer is discretized into $(L/a_0) \times (L/a_0)$ square elements, a_0 being the linear discretization so that the number of grid points in x and y direction are identical $n_x = n_y = L/a_0$. The Fourier transforms $\tilde{u}(q)$ are used as the dynamical degrees of freedom. Here, we employ the so-called mass-weighting GFMD variant as described in Ref. [27], because of its high convergence rate. The basic idea of mass-weighting is to assign inertia to each $\tilde{u}(\mathbf{q})$ mode such that the system's intrinsic frequencies collapse as well as possible. This can be achieved by choosing the inertia roughly inversely proportional to q. The equations of motion were augmented with a thermostat as described in Ref. [28] in order to introduce small, symmetry breaking perturbations to the displacement field. The thermal noise induces a quicker transition from an unstructured displacement field, $u(\mathbf{r}) \equiv$ const, to a structured one than round-off errors. The thermal energy is chosen very small so that it does not significantly assist the elastomer to overcome energy barriers. It is yet large enough to make the elastomer quickly "realize " when a displacement field is no longer stable against a small perturbation.

The mean gap, or in the case of Hertzian indenter, simply the displacement, is moved quasi-continuously using a ramp, which in most cases was realized as follows: For 50 time steps, u_0 is changed over a small quantum Δu_0. The system is then relaxed over typically 150 additional time steps. In most cases, this is sufficient to closely approach the next stable or metastable configuration. For a 512×512 system, one increment in average displacement then takes a little less than 1.5 seconds using our house-written GFMD code on a single core of a 1.6 GHz Intel Core i5 processor. For larger systems, the number of necessary time steps to be done per Δu_0 does not increase with system size due to the mass-weighting procedure.

3. Patterns and instabilities in periodically repeated, flat, adhesive contacts

Adhesion is known to lead to instabilities when two surfaces approach each other. The arguably simplest description of an adhesive instability was proposed by Tomlinson [29], who assumed atoms to be bonded to their lattice sites by springs of stiffness k. As a surface atom approaches a counterface, the position of the atom becomes unstable when the negative curvature of the atom-surface interaction exceeds k, at which case the atom jumps into contact. On retraction, the inverse jump occurs at an increased separation between the equilibrium site and the counter surface, so that hysteresis and thus energy dissipation results.

It is now well known that Tomlinson's model is not sufficiently refined to describe adhesive hysteresis. Its simplest valid description was proposed by Johnson, Kendall, and Robertson (JKR) [18]. In their solution of short-range adhesion in Hertzian contact geometries, jump to contact occurs at a zero load but breaking the same contact on retraction requires the tensile load and the work of adhesion to be finite.

Surprisingly little attention has been paid to flat, adhesive interfaces, unless they are nominally flat with true contact occurring only in isolated patches [30–33]. For surfaces in which microscopic roughness is not significant, previous studies [34,35] reveal that adhesive instabilities are easily triggered in the presence of a cohesive traction law, as to be expected from the JKR model in the limit of infinite radii of curvature. Yet, little has been reported on the jump into and snap out of contact for ideally flat adhesive surfaces, in particular when assuming periodic boundary conditions. In this section, we will be concerned with this question, not only for academic reasons (periodic boundary conditions do not exist in reality), but because this analysis gives clear cues on how to select mesh sizes and how to meaningfully modify CZMs when the mesh size cannot be made arbitrarily small. Towards this end, we use typical energy balance arguments, as originally done by Griffith [36] in the context of cracks and later by Maugis and Barquins [37] in the context of peeling, to describe the force-stress relations in certain asymptotic limits, while simulations are needed to properly describe those relations near instability points.

Fig. 2 shows the stress-displacement relation for a contact described by the two dimensionless numbers $L/\rho = 256$ and $\gamma/(E^*\rho) = 0.15$ along with patterns—as defined by the topography of the elastomer's surface—that arise as stable or metastable solutions. At very large separation, ideally flat surfaces are stable as shown in the inset (a) of Fig. 2. When approaching the indenter, the flat configuration becomes suddenly unstable, and a circular bulge, see inset (b), is formed. Upon further reduction of the mean gap, the bulge turns into a line ridge, depicted in inset (c). Next, the ridge develops into a dimple, as shown in inset (d). Finally, the elastomer's surface flattens out again at close approach as revealed in inset (e).

All transitions shown in Fig. 2 are reversible but discontinuous and thus hysteretic: upon retraction of the elastomer, the patterns reverse, however, at a larger mean gap than during contact formation. The areas between approach and retraction curve in the stress-displacement relation corresponds to the dissipated surface energy. In contrast to ordinary visco-elastic losses, the lost energy depends very weakly on the velocity $\dot{u}_0$ at small $\dot{u}_0$, see also Refs. [33,38,39] linking adhesive losses to (small-scale) instabilities rather than to visco-elastic effects. Since our simulations are thermostatted to a very small temperature, a minor logarithmic rate dependence of the lost energy with tiny prefactors is obtained.

Note that the patterns shown in the insets of Fig. 2 occurred at random locations of the simulation cell. However, they were moved to the center of the graphs for aesthetic reasons. Note also that the line ridge is formed parallel to x with the same probability as to y, however, it was never observed to form along the diagonal. To represent ridges consistently, we represented them parallel to y. Fig. 3 depicts the approach-retraction curve for a system, in which γ was kept the same as before, but L was increased to $L = 1024\,\rho$, i.e., to four times the linear dimension of the system represented in Fig. 2,

While surface patterns and instabilities show similarities for the two different system sizes, notable differences can be observed: in the larger system, the circular bulge has disappeared and instabilities span a broader range in the interfacial displacement than before. In addition, the energy hysteresis per

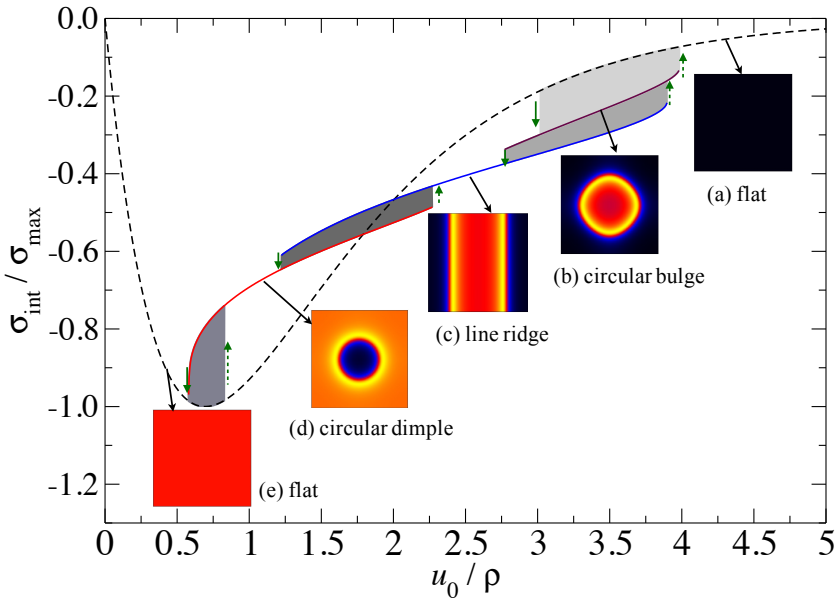

Figure 2. Mean stress (normalized to the maximum adhesive strength) as a function of mean displacement (in units of the interaction range) during approach (blue, upper solid curves) and retraction (red, lower solid curves). Four gray regions indicate the energy loss. The square insets show representative local, interfacial gaps on different branches, which increase from red to orange to yellow to blue to black. Solid and dashed red arrows indicate instabilities on approach and retraction, respectively. The dashed line indicates the stress-displacement relation for a flat elastomer.

unit area, $\gamma_{\rm hys} = \oint du_0 \sigma(u_0)$, has grown by a factor close to 4, which means that the total lost energy is still far from a linear scaling with system size for the used appropriate dimensionless numbers describing our system.

In the remaining part of this section, we attempt to rationalize and to quantify the differences for the different system sizes. This is done by two means, first by exploring a harmonic approximation around the stable or metastable, undeformed elastomer. This analysis provides a first guideline for how to set the minimum value for the range of adhesion in a cohesive-zone-model-based (peeling) simulation. Second, an energy analysis of the characteristic defect pattern is performed similar to the traditional Griffith analysis [18], however, adopted to periodically repeated domains. As a word of honesty, we must confess that we cannot fully judge to what extent Griffith theory of brittle fracture is simply "reinvented" in some of the following calculations, as we even find text books on that matter somewhat difficult to follow. If it is a reinvention, we hope to have provided an alternative derivation, which is easier to digest than common treatments of that matter, in particular because our treatment is based entirely on the (Fourier) stress-strain relation.

3.1. Harmonic approximation

At mean gaps, where an undeformed surface is the only stable solution, any deviation of the function $u(x,y)$ from $u(x,y) \equiv u_0$ is counteracted at fixed u_0 by a restoring force. For small perturbations, $\gamma(\mathbf{r})$ and therefore also $V_{\rm int}[u(\mathbf{r})]$ can then be expanded as a second-order Taylor series in the displacement so that the total excess energy w.r.t. a flat surface reads

$$\Delta V_{\rm tot} = \frac{A}{2} \sum_{\mathbf{q}, q \neq 0} \left\{ \gamma''(u_0) + \frac{qE^*}{2} \right\} |\tilde{u}(\mathbf{q})|^2 + \mathcal{O}(\delta u^3). \tag{5}$$

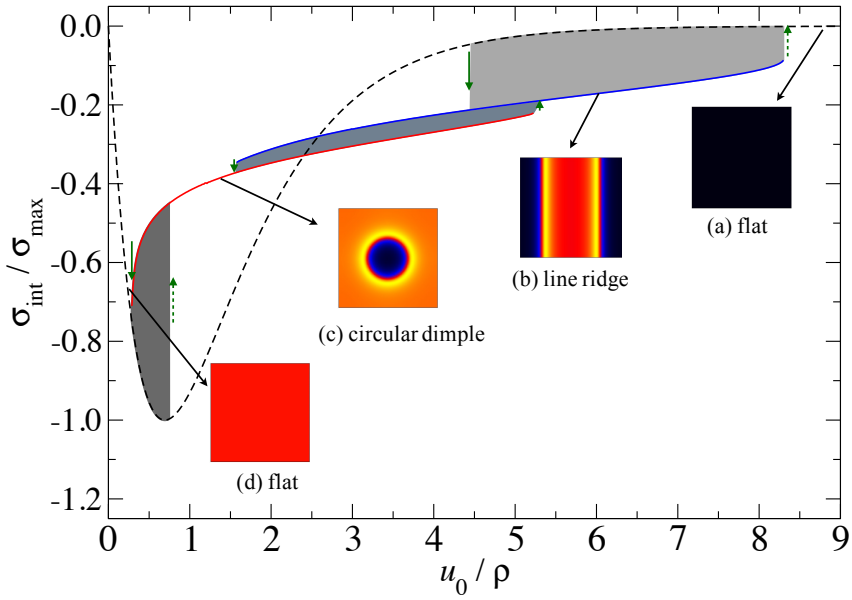

Figure 3. Similar to Fig. 2, however, for a linear system size of $L = 1024\,\rho$.

Thus, when $\gamma''(u_0)$ is negative, the harmonic approximation cannot be maintained if there exists a non-zero wave vector whose magnitude is less than the critical wave number

$$q_c(u_0) \equiv -2\gamma''(u_0)/E^*. \tag{6}$$

In other words, if the linear dimension of a periodically repeated cell exceeds a critical length

$$L_c = 2\pi/q_c, \tag{7}$$

the surface will deform spontaneously in response to a tiny perturbation of appropriate symmetry.

For fixed system size, two critical separations (may) result. For the used Morse potential, these can be evaluated to

$$u_c = -\rho \ln \left\{ \frac{1}{4} \pm \frac{1}{4}\sqrt{1 - \frac{4\pi\rho^2 E^*}{\gamma L}} \right\}. \tag{8}$$

Thus, for linear system sizes less than the critical size $L_c = 4\pi\rho^2 E^*/\gamma$, the undeformed surface can remain (meta) stable at any separation and instabilities can be avoided, even if configurations with lower potential energy may exist. Fig. 4 confirms that the just-made analytical calculations are consistent with the results of GFMD simulations.

3.1.1. Scale-dependent cohesive zone models

How do the just-obtained results relate to the construction of cohesive-zone models? Assume that a system is discretized to an in-plane linear dimension of a_0. If ρ were much less than the critical value below which a periodically repeated cell of length a_0 adopts internal defects, then a proper representation of the defect structure (e.g., a peeling front) cannot be represented. Subsequently, the energy required for the peeling process would be much too large. If, however, ρ were much in excess of the critical value, then the adhesion would become long ranged and potentially too long ranged for a given purpose, e.g., if a system had (microscopic) roughness, or the tape to be peeled were very thin. In that case, the force required to peel the system might be underestimated. This means that the

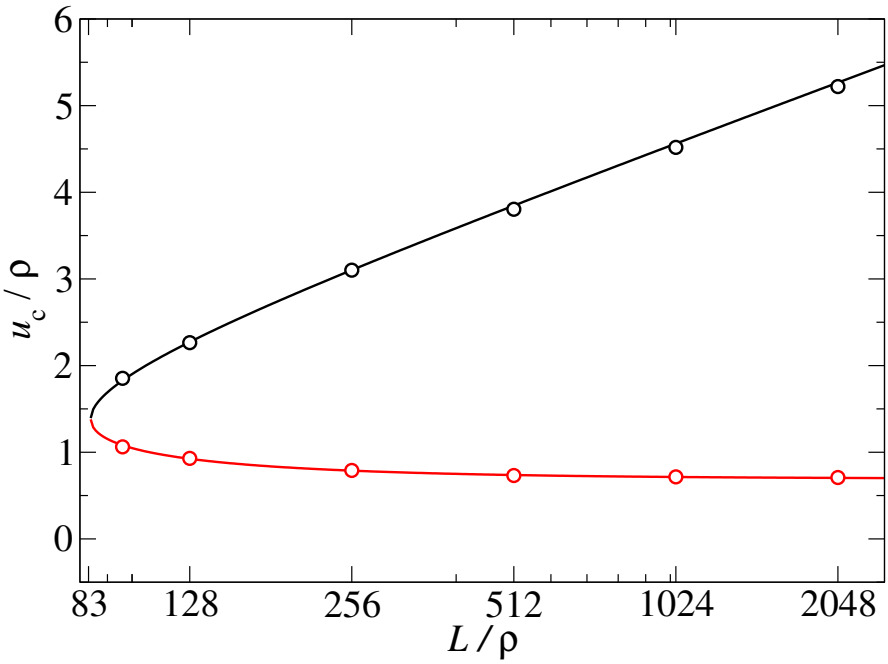

Figure 4. Critical separations at which an undeformed, flat surface becomes unstable. The upper (black) and the lower (red) branch relate to approach and retraction, respectively. Circles show GFMD simulation results, while lines reflect Eq. (8).

optimum choice for the mesh size, or, alternatively, the choice of the optimum range of interaction should satisfy

$$\rho \gtrsim \sqrt{\frac{\gamma\,\Delta a}{4\pi\,E^*}} \tag{9}$$

in the case of the Morse potential.

For a general CZM, the just-proposed criterion could also be formulated as

$$\min\left\{\gamma''(u)\right\} = -\mu_\rho^2 \cdot \frac{E^*}{\Delta a}, \tag{10}$$

where μ_ρ should be a constant of order unity. The precise optimum value for μ_ρ will depend on the specific functional form of the CZM, however, we do not expect a great sensitivity for reasonable choices. In the case of the Morse potential, Eq. (10) translates (back) to

$$\rho = \frac{1}{2\,\mu_\rho}\sqrt{\frac{\gamma\Delta a}{E^*}}. \tag{11}$$

3.2. *Griffith-based, continuum approach*

In this section, we identify some traction-displacement relations for mechanically stable or meta-stable, non-constant displacement fields. Thus, we attempt to minimize the total energy

$$V_{\text{tot}} = V_{\text{ela}} + V_{\text{int}} + V_{\text{ext}} \tag{12}$$

with respect to the displacement field, which contains an "external energy" V_{ext} in addition to the elastic and interaction energies, which have already been introduced. V_{ext} is the energy gained in response to an external load, including gravitational loads, i.e.,

$$V_{\text{ext}} = -p_{\text{ext}}\, u_0\, A \tag{13a}$$
$$= p\, u_0\, A \tag{13b}$$

where the external pressure p_{ext} plays the role of a Lagrange parameter, which is adjusted such that the desired mean displacement u_0 is an extremum of the total energy. The pressure p exerted from the indenter has the opposite sign of p_{ext} but is equal in magnitude.

In order to proceed analytically, adhesion is considered infinitesimally short ranged so that

$$V_{\text{int}} = -\gamma\, A_{\text{c}}, \tag{14}$$

where A_{c} is the real contact area.

In the following treatment, we will minimize the total energy per area. A lower-case letter v (with varying indices, i.e., ela, ext, int, and tot) will indicate that the pertinent energy is re-expressed as a surface energy density. Moreover, a periodically repeated square domain of length L will be assumed.

Since elasticity is a scale-free theory, in which energy increases quadratically with the displacement, and adhesion is considered infinitesimally short ranged, the mean total energy density of a given defect pattern must be of the form

$$v_{\text{tot}} = \frac{E^* u_0^2}{L}\, \hat{v}_{\text{ela}}(\alpha) + p\, u_0 - \gamma\, \hat{a}(\alpha), \tag{15}$$

where αL is the linear dimension of the non-contact with $0 < \alpha \leq 1$ so that $\alpha\, L$ would be, for example, the diameter of a dimple, Moreover, $\hat{v}_{\text{ela}}(\alpha)$ is a dimensionless function of α, while $\hat{a}(\alpha)$ denotes the relative contact area, i.e.,

$$\hat{a}(\alpha) = \begin{cases} \pi\, (\bar{\alpha}/2)^2 & \text{(bulge)} \\ \bar{\alpha} & \text{(ridge)} \\ 1 - \pi\, (\alpha/2)^2 & \text{(dimple)} \end{cases}, \tag{16}$$

where $\bar{\alpha} \equiv 1 - \alpha$ is the linear dimension of a contact patch in units of L.

The non-trivial part of the calculation is the determination of the function $\hat{v}_{\text{ela}}(\alpha)$. Asymptotic analytical solutions for some defect patterns are derived in the appendix for $\alpha \to 0$ and $\alpha \to 1$. They can also be determined numerically in adhesion-free simulations as described further below. For the moment, we simply assume the function $\hat{v}_{\text{ela}}(\alpha)$ to exist and to be differentiable.

For any stable solution, both u_0 and α must minimize the mean energy density, which is why the partial derivatives of v_{tot} with respect to these two variables must be equal to zero. Thus,

$$\frac{\hat{v}'_{\text{ela}}(\alpha)}{\hat{a}'(\alpha)} = \frac{\gamma\, L}{E^* u_0^2} \tag{17}$$
$$p = -\frac{2\, E^*\, u_0}{L}\, \hat{v}_{\text{ela}}(\alpha) \tag{18}$$

in mechanical equilibrium. A consequence of Eq. (17) is the existence of a maximum (or minimum) displacement u_0 if the l.h.s. of Eq. (17) has a minimum (or maximum).

Defining $\hat{\Xi}(...)$ such that $\alpha = \hat{\Xi}\{\hat{v}'_{\text{ela}}(\alpha)/\hat{a}'(\alpha)\}$ and inserting the resulting value of α into Eq. (18) yields

$$\tilde{p} = -2\, \tilde{u}_0^2\, \hat{v}_{\text{ela}} \left\{ \hat{\Xi} \left(\tilde{u}_0^{-2} \right) \right\}, \tag{19}$$

after expanding the fraction with u_0/γ. Here, we used

$$\tilde{u}_0 = \frac{u_0}{\sqrt{\gamma L/E^*}} \tag{20}$$

$$\tilde{p} = \frac{p}{\gamma/u_0}. \tag{21}$$

Thus, for any defect pattern, there is a unique shape of the $p(u_0)$ dependence in the continuum limit, which is obtained by expressing u_0 in units of $\sqrt{\gamma L/E^*}$ and p in units of γ/u_0.

The most important missing ingredient to identify the stress-displacement relation summarized in Eq. (19) is the determination of the dimensionless function $\hat{v}_{\text{ela}}(\alpha)$. For its numerical determination, we proceeded as follows: For a given defect pattern and a given fixed value of α, contact points were defined and constrained to a zero displacement. The energy is minimized with respect to the unconstrained displacement field under a given external pressure p_{ext}. In the last step, V_{ela} and u_0 are determined from $u(\mathbf{r})$. This was done for different discretizations, which allowed us to perform a Richardson extrapolation of the two observables of interest to the continuum limit for each value of α.

In the remaining part of this section, we will present our numerical results on $\hat{v}_{\text{ela}}(\alpha)$ and compare them to asymptotic results wherever appropriate as well as with simulation results that were obtained with finite-range adhesion. Since an accurate determination of $\Xi(\tilde{u}_0^{-2})$ turned out very labor intensive, we decided to abstain from this exercise for now.

3.2.1. Line ridge

The line ridge is considered first and with a greater level of detail than the other patterns, since it allows peeling to be studied in the most straightforward fashion. Periodic boundary condition make the simulation cell have two peeling fronts, which are mirror images of each other.

Two possible asymptotic limits arise, namely a thick ridge with a localized "line crack" as defect pattern for $\alpha \to 0$ and a thin contact ridge for α approaching unity from below as closely as possible. For each limit, it is possible to identify a closed-form analytical expression for $\hat{v}(\alpha)$:

$$\hat{v}_{\text{ela}}(\alpha) = \begin{cases} \frac{2}{\pi\alpha^2} & \text{(thick line ridge)} \\ \frac{\pi}{-4\ln(\pi\bar{\alpha})+8c} & \text{(thin line ridge)} \end{cases} \tag{22}$$

with $c = 0.3079(7)$. These two expressions are derived in appendices A.1 and A.2. Fig. 5 reveals that the analytical results for $\hat{v}_{\text{ela}}(\alpha)$ are consistent with GFMD data.

As mentioned before, u_0 has extrema (and thus end points) when the l.h.s. of Eq. (17) has an extremum. Since $\hat{a}'(\alpha) = -1$ for a line ridge, an endpoint of $u_0(\alpha)$ coincides with an extremum in $\hat{v}'_{\text{ela}}(\alpha)$. Since $\hat{v}'_{\text{ela}}(\alpha)$ is monotonic at small α, no unstable point exists in the continuum solution for thick line ridges. Thus, the instabilities in the GFMD simulations toward the formation of dimples can only have arisen due to adhesion having been modeled with a finite range. The power-law relation

$$\alpha = \left(\frac{4E^* u_0^2}{\pi L \gamma}\right)^{1/3}, \tag{23}$$

is easily deduced in the $\alpha \to 0$ thick-ridge limit, which turns out to be quite accurate even up to $\alpha \lesssim 0.7$ as evidenced in Fig. 6.

In contrast to the thick-line-ridge limit, the thin-line-ridge asymptote *does* have a critical value α_c, at which $\hat{v}_{\text{ela}}(\alpha)$ has zero curvature. It is located at $\alpha_c \approx 0.92(0)$. Although the thick-line-ridge limit appears to match α_c quite well, it fails to produce a truly satisfactory $p(u_0)$ dependence, because the first and the second derivative are not quite as accurate as $\hat{v}_{\text{ela}}(\alpha)$ itself.

In order to obtain a more precise estimate for the asymptotic thin-ridge behavior before the instability to flattening, GFMD calculations of the reduced elastic energy were refined in the vicinity

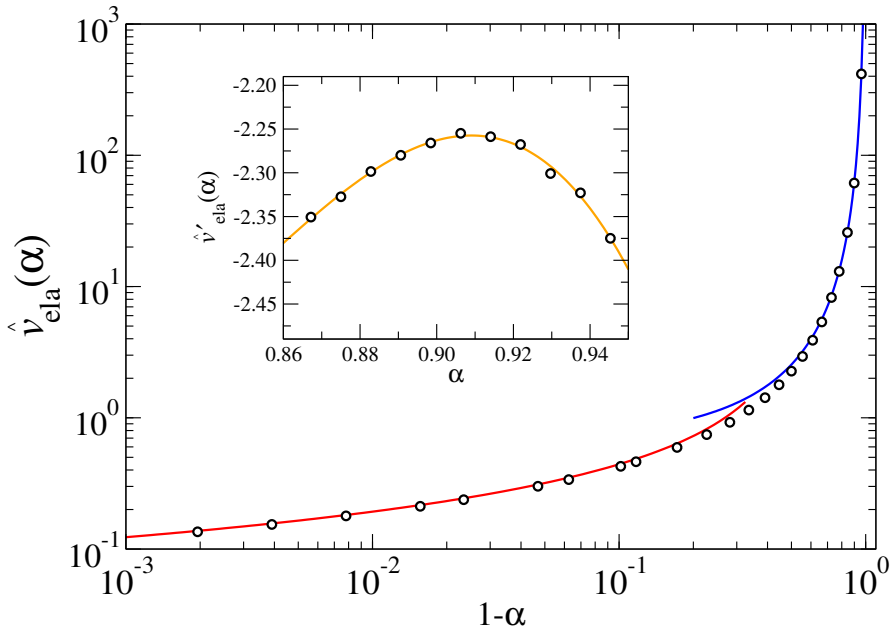

Figure 5. Dimensionless elastic energy $\hat{v}_{\mathrm{ela}}(\alpha)$ for a line ridge as a function of $1-\alpha$. Symbols show GFMD results. The red and blue lines reflect the $\alpha \to 1$ and $\alpha \to 0$ asymptotics respectively. Inset: $\hat{v}'_{\mathrm{ela}}(\alpha)$ in the vicinity of its maximum. The orange line shows a third-order polynomial of α.

of α_{c}. The following results were deduced, which allow that "critical behavior" to be characterized: $\alpha_{\mathrm{c}} = 0.90(9)$, $\hat{v}_{\mathrm{c}} \equiv \hat{v}_{\mathrm{ela}}(\alpha_{\mathrm{c}}) = 0.420(4)$, $\hat{v}'_{\mathrm{c}} \equiv \hat{v}'_{\mathrm{ela}}(\alpha_{\mathrm{c}}) = -2.2(6)$, and $\hat{v}'''_{\mathrm{c}} \equiv \hat{v}'''_{\mathrm{ela}}(\alpha_{\mathrm{c}}) = -1.4(5) \cdot 10^2$. Thus, near the flattening transition, Eq. (17) reads

$$-\hat{v}'_{\mathrm{c}} - \frac{\hat{v}'''_{\mathrm{c}}}{2}(\alpha - \alpha_{\mathrm{c}})^2 = \frac{1}{\tilde{u}_0^2}, \tag{24}$$

in leading order, which can be easily solved for $\alpha(\tilde{u}_0)$. Just before the flattening instability, a critical separation of $\tilde{u}_{\mathrm{c}} = 1/\sqrt{-\hat{v}'_{\mathrm{c}}} \approx 0.665(6)$ is reached.

The final analytical step is to insert the two analytical $\alpha(u_0)$ dependencies into Eq. (18). In the thick-line-ridge limit, this yields

$$\frac{p}{E^*} = -\left(\frac{4\gamma^2}{\pi L E^{*2} u_0}\right)^{1/3}, \tag{25}$$

which reads

$$\tilde{p} = -\sqrt[3]{4/\pi}\,\tilde{u}_0^{2/3} \tag{26}$$

in reduced variables. In the thin-line-limit, we obtain in leading order

$$\tilde{p} = \tilde{p}_{\mathrm{c}} + \tilde{p}_{\mathrm{c}}^{(1/2)}\sqrt{\tilde{u}_{\mathrm{c}} - \tilde{u}_0} \tag{27}$$

with $\tilde{p}_{\mathrm{c}} \approx -0.393(7)$ and $\tilde{p}_{\mathrm{c}}^{(1/2)} = -2/\tilde{u}''_{\mathrm{c}}(\tilde{p}_{\mathrm{c}}) \approx -0.360(0)$.

Fig. 7 reveals the correctness of our analysis. The larger system with fixed finite-range adhesion reproduces the continuum solution more closely than the smaller system. This includes a closer approximation of the end-points.

The continuum solution shown in Fig. 7 is an overlapping superposition (conglomerate) of three different approaches: On $0 \le \alpha \le 0.1$ and on $0.6345 \le \alpha \le \alpha_{\mathrm{c}}$ the thick-line-ridge asymptotic solution and the expansion about the flattening point are depicted, respectively. In addition, the GFMD data presented in Fig. 5 was processed numerically to yield results on $0.05 < \alpha < 0.663$. It agrees with the two shown approximations within line widths in the shown overlapping domains.

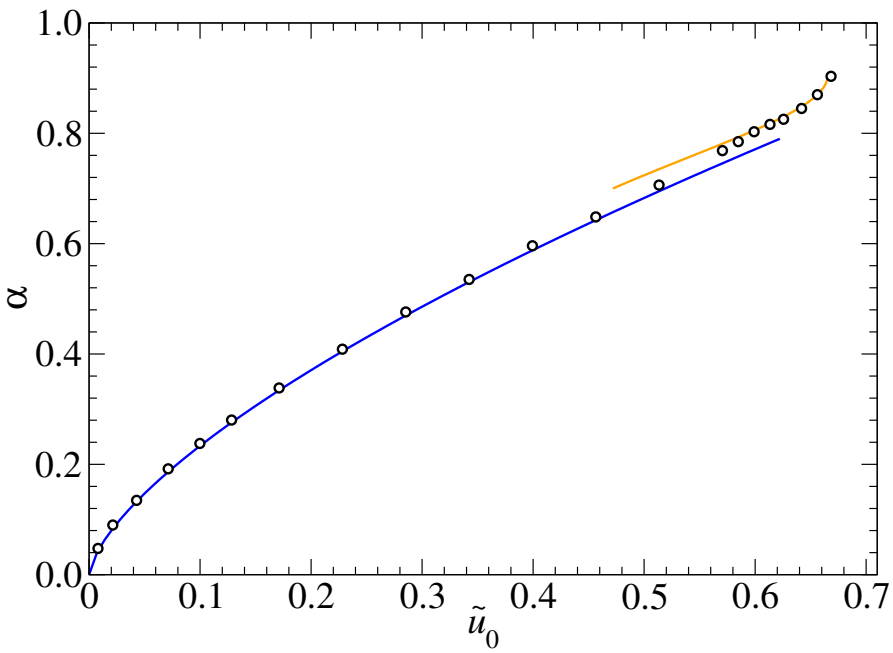

Figure 6. Comparison of the $\alpha(\tilde{u}_0)$ dependence obtained with GFMD to the asymptotic thick-ridge (blue line) and critical point (orange line) solutions.

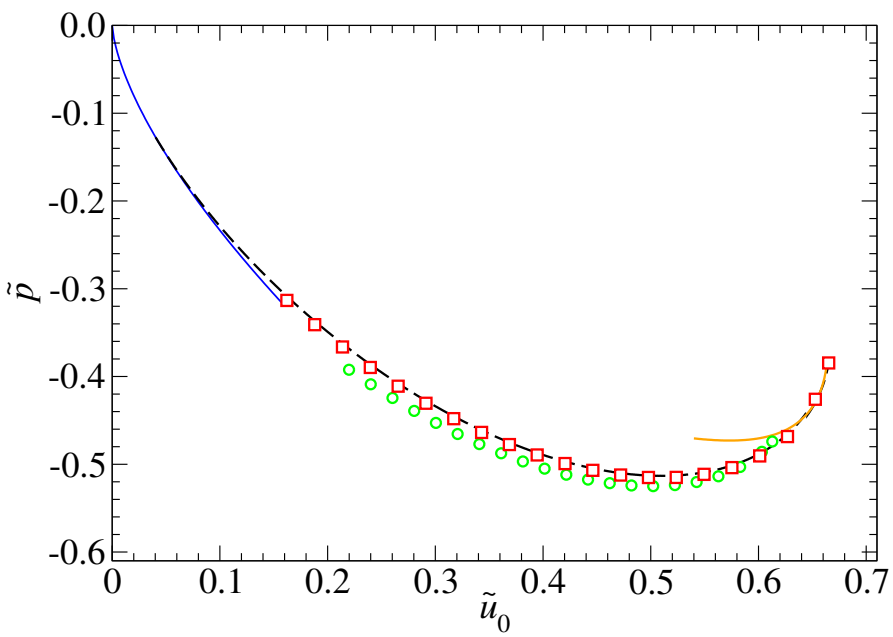

Figure 7. Reduced pressure $\tilde{p} \equiv p/(\gamma/u_0)$ as a function of reduced displacement $\tilde{u}_0 \equiv u_0/\sqrt{\gamma L/E^*}$ for different values of $\tilde{\rho} \equiv \rho/\sqrt{\gamma L/E^*}$, i.e., for $\tilde{\rho} = 0.1614$ (green, small circles) and $\tilde{\rho} = 0.0807$ (red, large squares). For these calculations, dimples were suppressed by making the cell in the y direction infinitesimally thin. The full blue and the full orange line represent the thick-line and critical-point asymptotics, respectively, while the dashed black line shows a direct numerical analysis of the GFMD data from Fig. 5.

We now turn our attention back to a computational question central to this study. How can we design a CZM such that it reproduces the $\tilde{p}(\tilde{u}_0)$ relation for zero-range adhesion as accurately as possible for a given, fixed number of grid points. In Sect. 3.1.1, a scaling relation was proposed towards this end, which is tested next. Fig. 8 reveals that using $\mu_\rho \gtrsim 0.5$ induces instabilities and thus hysteresis on the $p(u_0)$ curve, which do not exist in the continuum solution and which would disappear if ρ was kept constant but the mesh was refined. For $\mu_\rho \lesssim 0.5$, instabilities disappear but only a relatively small part of the line-ridge solution is stable for the given discretization of $n_x = 16$.

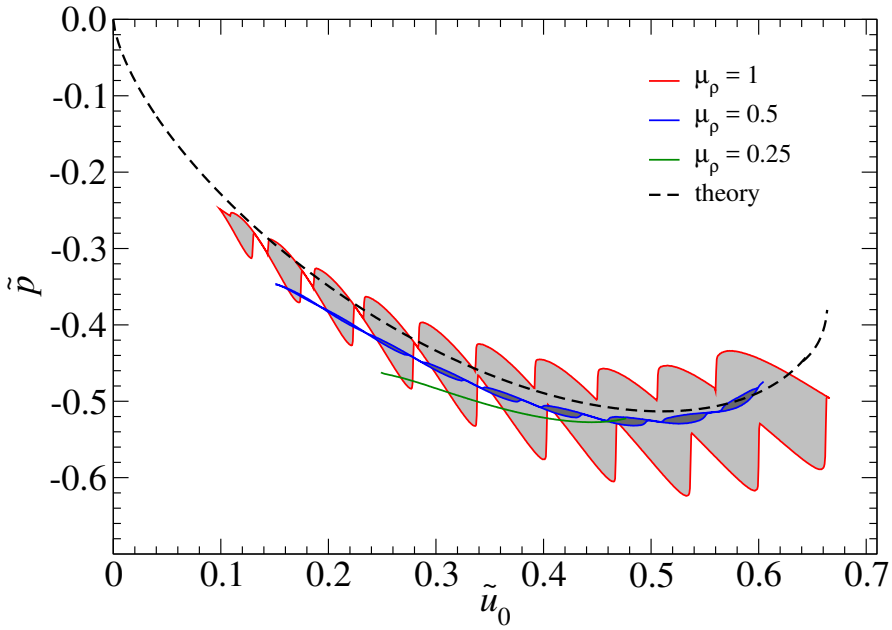

Figure 8. Reduced pressure $\tilde{p}$ as a function of reduced displacement $\tilde{u}_0$ for a fixed mesh of $n_x = 16$ grid points in x-direction. For these calculations, dimples were suppressed by making the cell in the y direction infinitesimally thin. Different scaling parameters μ_ρ determining the range of interaction were used.

Despite visible discrepancies, the agreement between the exact solution and the one obtained for $\mu_\rho = 0.5$ can be called surprisingly good, because the discretization of the simulation cell into $n_x = 16$ elements disposes only of eight independent, i.e., symmetry-unrelated points to describe contact plus non-contact. They both have fields (stress and derivative of displacement) that cannot be Taylor expanded upon. This makes a total of four fields, which are numerically difficult to integrate, because the simulation cell contains two peeling processes, plus the zones in between the diverging fields. Their combined effect is reflected by merely 16 grid points. Anyone having applied numerical integration schemes to such "poorly behaved" functions will thus certainly appreciate the "performance" of the $n_x = 16$, $\mu_\rho = 0.5$ simulation. Specifically, for $\mu_\rho = 0.5$, the line ridge becomes unstable to flattening at $\tilde{u}_0 \approx 0.15$ for a thick ridge (dimples were suppressed by using $n_y = 1$ for the analysis of ridges) and at $\tilde{u}_0 \approx 0.6$ for a thin ridge. From Fig. 6, it becomes obvious that non-contact is only about 30% of the simulation cell in the first case and contact is only 20% of the simulation cell in the second. At that point, a simulation effectively evaluates an integral over displacement (first case) or stress (second case) field using only two to three integration points. Yet relative errors are relatively small. They decrease quite substantially for all three studied choices for μ_ρ when the linear mesh size is reduced to half its value. Evidence for this claim is not shown explicitly, because the main problem is the approach *to contact* rather than a proper description of $p(u_0)$ *in contact*, as will be discussed further below.

3.2.2. Circular defect patterns

Since our main interest is the line ridge, we only sketch results for the two remaining defect patterns. The dimensionless elastic energy for the two circular patterns satisfies

$$\hat{v}_{\text{ela}}(\alpha) = \begin{cases} \frac{8}{\sqrt{3}\pi\,\alpha^3} & \text{dimple, } \alpha \to 0 \\ \sqrt{2}(1-\alpha)^{3/2} & \text{bulge, } \alpha \to 1. \end{cases} \tag{28}$$

Fig. 9 shows the numerical results for $\hat{v}_{\text{ela}}(\alpha)$ of the two circular defects including their asymptotic behavior.

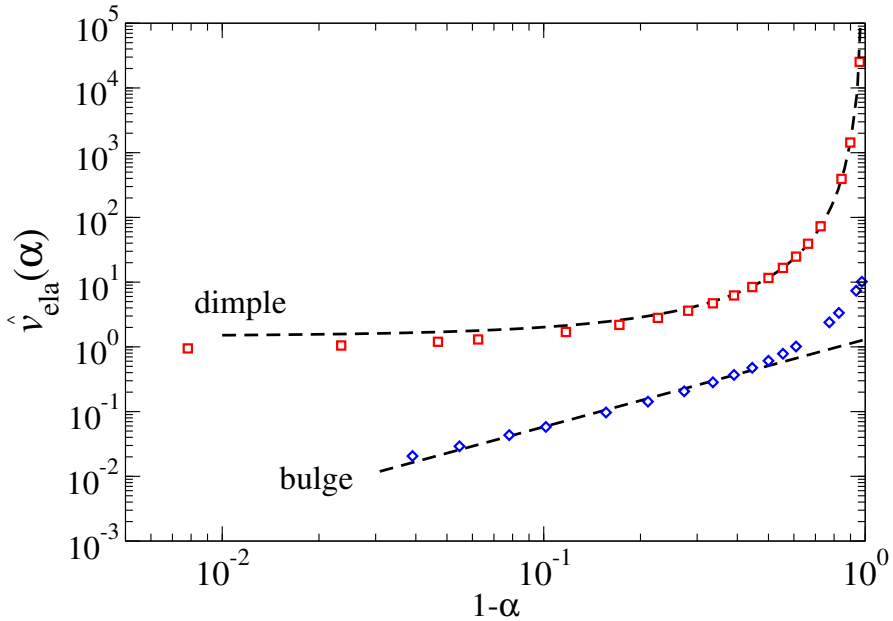

Figure 9. Dimensionless elastic energy $\hat{v}_{\text{ela}}(\alpha)$ as a function of the relative, linear contact dimension $\bar{\alpha}$ for the dimple (red squares) and the bulge (blue diamonds).

Proceeding as above, the $\tilde{p}(\tilde{u}_0)$ is obtained as

$$\tilde{p} = -\left(4\tilde{u}_0/3\right)^{4/5} \tag{29}$$

for the dimple. Fig. 10 reveals that this asymptotic solution is approached as the (dimensionless) range of adhesion is reduced.

No stable solution exists for the bulge in the continuum limit, because an extremum in $v_{\text{tot}}(\alpha)$ is a maximum in α. Thus, the bulge in Fig. 2 can only have arisen as a consequence of the finite-range of the adhesion. This argument is supported by the bulge's disappearance in Fig. 3, in which the (dimensionless) range of adhesion was reduced compared to that used in Fig. 2. It is also consistent with the observation that the detachment process of a nominally flat surfaces (which can be roughly mimicked with—or "coarse-grained" to—Morse-like potentials) frequently has one last contact patch in place before the contact breaks.

3.3. Dissipated energy

When two or more stable microstates coexist for a given collective degree of freedom, quasi-discontinuous transitions between them occur when the collective degree is driven externally. This is the mechanism by which multistability leads to instability and ultimately to energy loss, which, as stated in Coulomb's law of friction, predominantly depends on the moved distances and much less on rates or velocities [29,40]. For Coulomb's friction law and related laws to be applicable, the motion

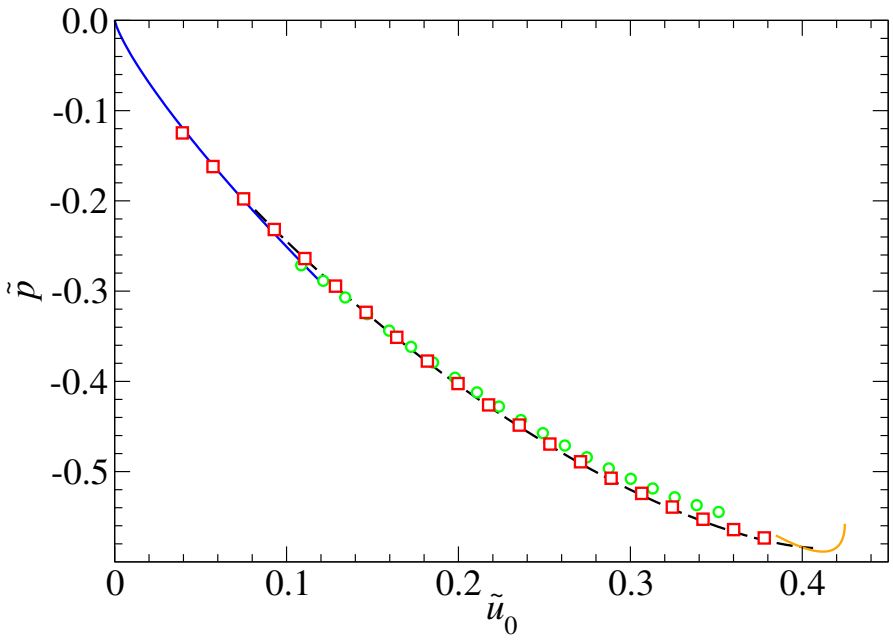

Figure 10. Reduced pressure $\tilde{p}$ as a function of reduced displacement $\tilde{u}_0$ for different values of $\tilde{\rho}$. i.e., for $\tilde{\rho} = 0.1614$ (small, green circles) and $\tilde{\rho} = 0.0807$ (large, red squares). The full blue and the full orange line represent the point-dimple and critical point asymptotics, respectively, while dashed black line shows a direct numerical analysis of the GFMD dimple data from Fig. 9.

has to be slow enough to prevent "basin hopping" between the two stable "macro" states when they are similar in energy but not so fast that significant heating occurs. In this section, we calculate the energy hysteresis arising from the multistability of non-contact and a line ridge.

In a first approximation, the stress can be approximated with zero as long as the elastomer is flat. The approximation is exact for potentials with a true cut-off, as for example, in the potential introduced later in Eq. (31). When the range of adhesion is very small, the elastomer turns directly to a thick line ridge upon approach, which happens at the distance $u_{\mathrm{c,\,nc}}$, where the flat, non-contact solution becomes unstable. It is the larger of the two solutions in Eq. (8), that is, the one in which the minus sign is selected in the parenthesis on the r.h.s. of that equation. Upon retraction the elastomers flattens out again at the critical distance, $u_{\mathrm{c,lr}}$, where the line-ridge solution becomes unstable. Thus, for short-range adhesion

$$\oint du_0\,\sigma(u_0) \approx \int_{u_{\mathrm{c,nc}}}^{u_{\mathrm{c,lr}}} du_0\,\sigma_{\mathrm{lr}}(u_0) \tag{30a}$$

$$\approx \frac{3}{2}\left(\frac{4\gamma^2 E^*}{\pi L}\right)^{1/3} u_0^{2/3}\Bigg|_{u_0=u_{\mathrm{c,nc}}}^{u_{\mathrm{c,r}}} \tag{30b}$$

$$\approx \frac{3}{2}\,\alpha_{\mathrm{c}}\,\gamma - \frac{3}{2}\left(\frac{4\gamma^2 E^*}{\pi L}\right)^{1/3} u_{\mathrm{c,nc}}^{2/3} \tag{30c}$$

$$\text{(for Morse)} \approx \frac{3\gamma}{2}\left\{\alpha_{\mathrm{c}} - \left(\frac{2\tilde{\rho}}{\sqrt{\pi}}\ln\frac{2}{\pi\tilde{\rho}^2}\right)^{2/3}\right\}. \tag{30d}$$

is obtained in a cycle going from non-contact to line ridge and back to non-contact.

In a more refined calculation, the "integration constant" $3\,\alpha_{\mathrm{c}}/2$ can be replaced with a more precise value for the lost energy in the continuum limit. The latter is best obtained by integrating (numerically) the $p(u_0)$ curve that is reconstructed from the reference line shown in Fig. 7. Moreover, a correction of $v_{\mathrm{int}}(u_{\mathrm{c,nc}}) - v_{\mathrm{int}}(u_{\mathrm{c,lr}})$ due to the gained energy while approaching the counterface in non-contact must be subtracted from the dissipated energy to yield accurate estimates.

The second term on the r.h.s. of Eq. (30c) is the main correction to the dissipated energy that arises by replacing a zero-range with a finite-range adhesion. Unfortunately, convergence of the computed dissipated energy is rather slow. For CZMs with a true cutoff g_c linear in ρ, the error disappears with $\rho^{2/3}$ and thus with $\Delta a^{1/3}$. For the Morse potential, this scaling is further impeded by corrections logarithmic in ρ. GFMD data confirm these conclusions in Fig. 11.

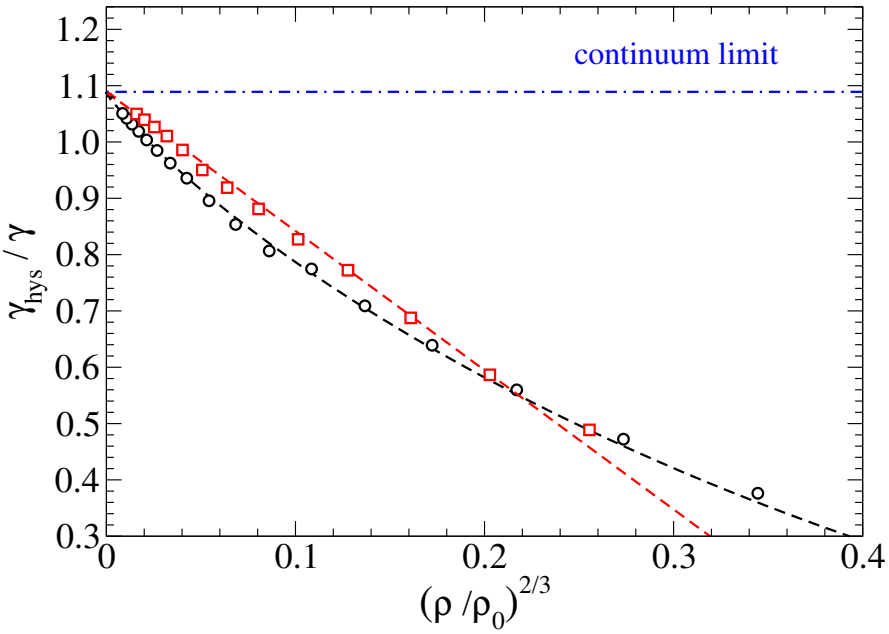

Figure 11. Normalized dissipated energy γ_h/γ as a function of the dimensionless range of interaction ρ/ρ_0 with $\rho_0 = \sqrt{\gamma L/(4\pi E^*)}$. The red and black dashed lines show the theoretical line derived from Eq. (30c) — plus the contribution $\gamma(u_{c,nc}) - \gamma(u_{c,r})$ for the Morse potential. Circles and squares indicate GFMD results for Morse potential and cosine potential, respectively. The blue line gives the asymptotic value derived from the analysis of the dashed line in Fig. 8.

Since optimizing prefactors is particularly important when convergence is slow, it may be desirable to use other CZMs than the one based on the Morse potential. For a CZM used to study not only (quasi-) statics, as in this work, but true dynamics, an additional requirement would be that the stress is a continuous function of the interfacial separation. This is because (strongly) discontinuous forces or stresses, as they occur in many CZMs at small g_c [3,4,10,11,14], violate energy conservation even for symplectic integration scheme [41]. This in turn is likely to lead to undesirable dynamical artifacts, e.g., when modeling reciprocating motion. A simple CZM avoiding discontinuous forces is:

$$\gamma_{\cos}(g) = -\gamma \times \begin{cases} 0 & \text{for } g_c < g \\ \frac{1}{2}\left\{1 + \cos\left(\pi g/g_c\right)\right\} & \text{for } 0 < g < g_c \\ \left\{1 - \left(\pi g/g_c\right)^2/2\right\} & \text{for } g < 0. \end{cases} \tag{31}$$

Fig. 11 reveals that the alternative CZM converges to its asymptotic value more quickly than the Morse potential. Even more importantly, extrapolation to short-range adhesion can be achieved already at relatively large interaction ranges. This is mainly because the alternative CZM lacks the corrections in the second term on the r.h.s. of Eq. (30d) that are logarithmic in $\tilde{\rho}$.

4. Application to Hertzian contacts

In this section, we explore to what extent the insights gained for adhesive hysteresis and the modeling of adhesive hysteresis in ideally flat contacts extend to uneven surfaces. To this end, we simulate adhesive contacts with Hertzian indenters. While our initial motivation for these simulations

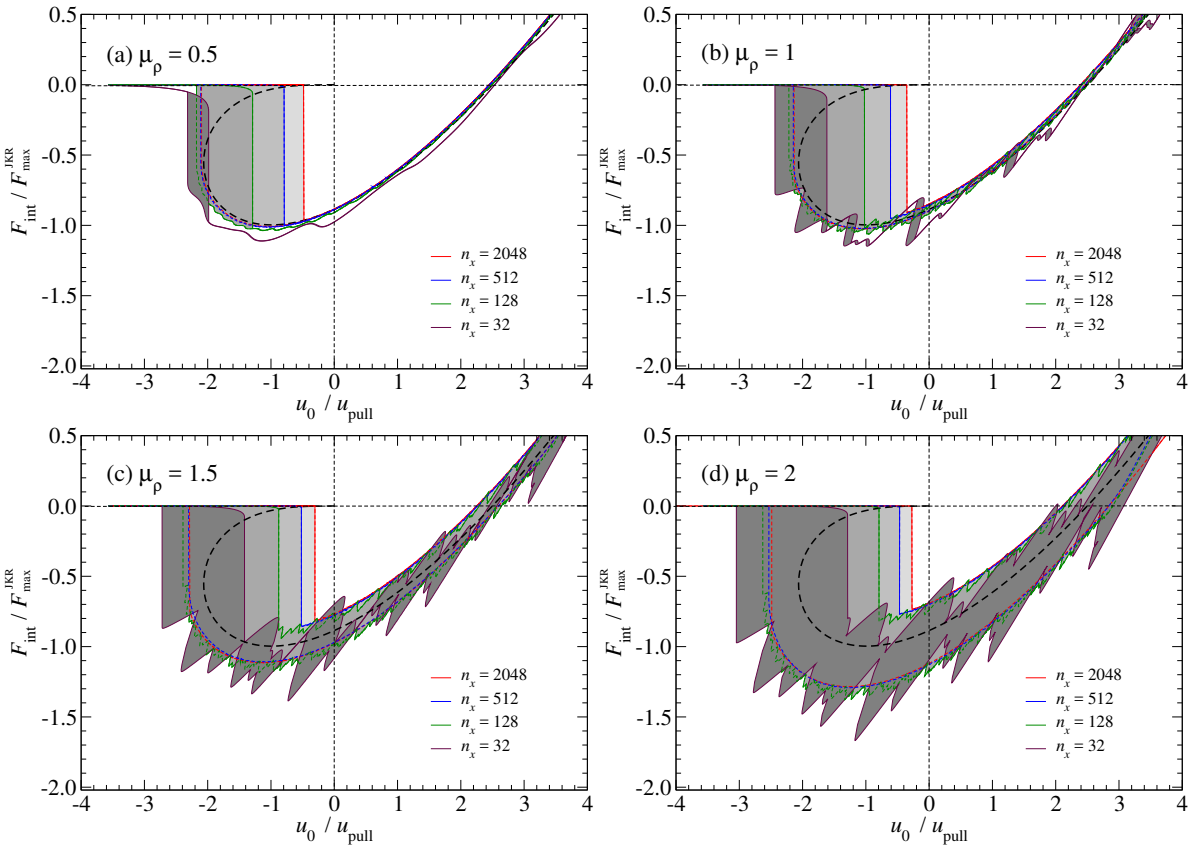

Figure 12. Typical traction-separation curves for adhesive Hertzian indenters with different discretization n_x and different scaling factors μ_ρ determining the range of interaction through Eq. (11). (a) $\mu_\rho = 0.5$, (b) $\mu_\rho = 1$, (c) $\mu_\rho = 1.5$, and (d) $\mu_\rho = 2$. The used cell dimension L was identical to the radius curvature R_c.

was to explore how the continuum limit can be approached in the most effective way, it is also possible to look at these calculations as if the used CZMs had arisen from integrating out the effect of small-wave-length surface undulations, i.e., from wave lengths much less than either the contact radius in a Hertzian contact geometry or less than the short wave length cutoff in the simulation on nominally flat surfaces.

We consider a Hertzian contact with radius of curvature R_c and contact modulus E^*, which define the units for length and pressure, respectively. The interfacial energy density, as defined in Eq. (3), is assigned the value of $\gamma = 0.59 \cdot 10^{-3}\, E^*\, R_c$. This choice makes the critical contact radius at the pull-off instability be roughly 10% of the radius of curvature, which was also used as the linear size of the periodically repeated simulation cell. This way, the contact radius is small compared to half a cell dimension so that the periodic boundary conditions have a marginal effect on the contact, while, at the same time, a Fourier-based code remains efficient. Using the definition of the Tabor parameter μ_T as in Eq. (8) of Ref. [42], the relation between μ_T and μ_ρ is

$$\mu_T = 2\,\mu_\rho \left(\frac{\gamma}{R_c E^*}\right)^{1/6} \sqrt{n_x}, \tag{32}$$

which turns out to be $\mu_T \approx 0.579 \cdot \mu_\rho \sqrt{n_x}$ for the used parameters. This relation is useful to know for our later analysis. Moreover, we define the displacement such that a flat elastomer, which touches the indenter in its most extreme point is assigned a (mean) displacement of $u_0 = 0$.

Fig. 12 compares the displacement-driven force-distance dependence in approach and retraction for different choices of μ_ρ and varying mesh sizes $\Delta a = L/n_x$. Qualitatively different types of behaviors

are produced by using different numerical values for μ_ρ in Eq. (11): (a) If μ_ρ is small, i.e., less than 0.5, the only observed instabilities are collective jump-into and jump-out-of contact. In this case, the hysteresis compared to the exact solution is strongly underestimated at a coarse discretization, however, the true hysteresis is approached when increasing n_x. (b) As μ_ρ increases to values around unity, small-scale instabilities occur, which are related to individual rings of (coarse-grained) atoms. The correct hysteresis is still approached, because instabilities on the compressive branch become smaller with increasing n_x. (c) As μ_ρ increases to 1.5, the computed dissipated energy in a compression/decompression cycle starts to depend quite sensitively on how far the system is compressed, e.g., if it is compressed to a zero displacement or to a zero load. For $\mu_\rho = 1.5$, it is not clear if convergence to the continuum limit can be reached. (d) For even larger μ_ρ, small-scale instabilities dominate and both pull-off force as well as dissipated energy no longer converge to the correct values as the mesh size is decreased.

The results presented in Fig. 12 ressemble to a significant degree simulations of contacts involving a curved ridge to which a single-sinusoidal undulation is added, see Figs. 5–7 in Ref. [38]. In those figures, the force-displacement relation also transits from subtle perturbations of a smooth JKR dependence to violent zig-zag motion. Differences are that our undulations arise from discreteness effects while those in Ref. [38] are due to continuous undulations. Moreover, spacings between discontinuities are irregular in our case but regular in Ref. [38], as our system is two-dimensional, in which case rings of discretization points have irregular spacings, which, moreover, become smaller and smaller the greater the distance from the symmetry axis.

An interesting feature revealed in Fig. 12 is that the JKR separation curve can be approximated quite well with Tabor parameters as small as $\mu_\mathrm{T} \approx 1.6$, as evidenced by the $n_x = 32$ curve in Fig. 12(a). In fact, for $\mu_\mathrm{T} = 4$, both the dependence of contact area and of displacement on load are almost indistinguishable from the exact JKR solution [7] when using large n_x but fixed μ_T. However, the approach curve is still relatively crude even when the Tabor parameter is as large as $\mu_\mathrm{T} \approx 10$, i.e., for the ($n_x = 256$, $\mu_\rho = 1$) data set shown in Fig. 12(b).

To further discuss the ramifications of Fig. 12, it is useful to know that the critical contact radius in a load-driven separation is $a_\mathrm{c} \approx 0.1278\, R_\mathrm{c}$ for the parameters used, which reduces to roughly half that value of $a_\mathrm{c} \approx 0.06315\, R_\mathrm{c}$ in a displacement-driven separation. Thus, to obtain estimates within approximately 20% accuracy for pull-off stress and dissipated energy density, the length into which the elastomer is discretized should not exceed $a_\mathrm{c}/10$ for the given value of $\gamma/E^* R_\mathrm{c} = 0.5859 \cdot 10^{-3}$. This is a finer discretization than for non-adhesive contacts, where we observe an error of order 10% in the normal displacement for a linear mesh size of $\Delta a = a_\mathrm{c}/5$.

We next quantify the effect of mesh size on the pull-off force F_pull and on the energy, $V_\mathrm{hys} = \oint du_0 F(u_0)$, dissipated in a single c/d cycle. Due to the presence of micro-scale instabilities during contact, V_hys does not have a unique value but depends on the maximum displacement during the compression cycle. We chose it to be the displacement at which the normal load, needed to keep the elastomer at a fixed center-mass, disappeared. In other words, V_hys corresponds to be the gray-shaded areas in Fig. 12 below the x-axis times the maximum JKR tensile force to which F_pull was normalized. Results for F_pull and V_hys are shown in Fig. 13.

The adhesive Hertzian indenter shows similar behavior as the flat-on-flat geometry in the following ways: the dissipated energy converges noticeably slower to its asymptotic value than the pull-off force. The scaling factor μ_ρ has to be sufficiently small in order for convergence to the correct values to be reached. For large μ_ρ, results are quite insensitive to the mesh size Δa. For Hertzian contact geometries, we did not repeat the simulation by replacing the default Morse expression for the surface energy, $\gamma(g)$, with $\gamma_\cos(g)$. However, we are certain that convergence to the continuum limit can been reached more quickly with this alternative form. Preliminary analysis on hysteresis in nominally flat contacts also indicates the scaling identified for the flat-on-flat geometry.

We note that it can be difficult to judge if the use of a given $\mu_\rho > 0.5$ is not too "aggressive". The data for $\mu_\rho = 1.5$ shows the correct trends in the sense that the F_pull decreases and V_hys increases

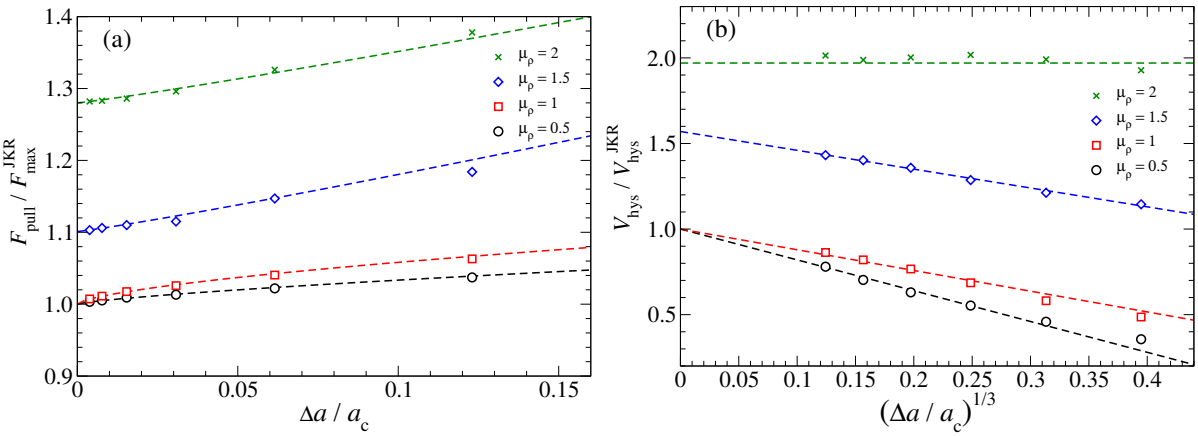

Figure 13. Maximum tensile force F_{pull} and dissipated energy V_{hys} as a function f the mesh size Δa. F_{pull} and V_{hys} are normalized to the values deduced from the JKR solution, while Δa is normalized to the critical JKR contact radius in a displacement driven separation.

with decreasing mesh size Δa. However, neither asymptotic quantity converges to its exact value, which can be deduced from the JKR solution, even if errors are not large. Thus, to be sure about the asymptotic values, either μ_ρ has to be chosen sufficiently small from the beginning, or it has to be set to two different numbers, which then yield identical asymptotics.

5. Conclusions and Outlook

The three main aims of this paper were (i) to provide a comprehensible theoretical framework describing the formation and failure (brittle fracture) of an adhesive, periodically repeated interface under constant normal stress and the subsequent energy hysteresis, (ii) to deduce generally applicable rules for the construction of cohesive-zone models from the theoretical framework, and (iii) to apply the schemes obtained for the contact between two ideally flat surfaces to uneven surfaces.

A particular focus of our work was the much overlooked approach to contact and the question at what separation an initially flat elastomer approaching a substrate with short but finite-range adhesion becomes unstable to the formation of surface ondulations. This happens when the negative curvature of a cohesive-zone model (CZM) exceeds $qE^*/2$, where q is the wavenumber associated with a surface undulation. The ramification for the numerical modeling is that a mesh size should not exceed the scale within which an elastomer would want to ripple during the approach to contact, which leads to the condition

$$\max\left\{-\gamma''(g)\right\} \lesssim \frac{E^*}{\Delta a}, \tag{33}$$

Δa being the mesh size of an element into which the surface is discretized. This inequality can be used to either define the mesh size or to (re)define the CZM. In this work, we used it to set the range of interaction ρ in a CZM whose functional form was that of the Morse potential, which yields the proportionality $\rho \propto \sqrt{\gamma \Delta a / E^*}$. Using a proportionality factor of $\mu_\rho = 0.5$, see also Eq. (11), no undesired instabilities show on the approach curve, while they do occur for $\mu_\rho = 1$.

The usual procedure when modeling adhesive contacts is to ask the question at what tensile stress a mesh element is going to detach [4,10,43]. The common argument is that it does so when the energy released during the detachment process exceeds the work of adhesion, which in turn leads to the condition $\sigma_{\text{tens}}^{\max} \approx \sqrt{2E^*\gamma/\Delta a}$, which—when applied to a continuous, twice differentiable CZM—can be readily translated to Eq. (33). Table 1 gives a summary of choices made by different authors, however, translated to the proportionality factor μ_ρ used for the Morse potential.

A compromise needs to be made when choosing the prefactor μ_ρ. For the approach curve, the proportionality factor is chosen at best as small as possible. However, when it is made too small,

Table 1. Values for μ_ρ implicitly used in different cohesive zone models.

model	year	μ_ρ
Dugdale [3]	(1960)	0.798
Hillerborg [12]	(1976)	0.5
Irwin [13]	(1997)	0.886
Falk *et al.* [14]	(2001)	0.532
Hui *et al.* [15]	(2003)	1.09
Popov *et al.*[16,17]	(2015)	0.729

artificial instabilities and thus energy hysteresis ensue that are not present on the continuum solution. Unfortunately, if the proportionality factor is above a critical value, the continuum solution cannot be reached even for $\Delta a \to 0$. Thus, a relatively safe choice should be to set the prefactor such that a flat-on-flat geometry reveals no undesired instabilities. It appears as if excellent choices have been made in the literature so that the range of interaction is made small enough to lead to the (almost) best possible convergence while being large enough to converge to the correct value.

The trouble of Eq. (33), as it comes to modeling adhesion in the zero-range or continuum limit, is that the range of adhesion can only be chosen as $\rho \propto \sqrt{\Delta a}$. This poor scaling is particularly problematic for the determination of adhesive hysteresis, because the lost energy density γ_{hys} scales only with $\rho^{2/3}$ so that γ_{hys} has corrections that cannot disappear more quickly than with $O(\sqrt[3]{\Delta a})$, which for a two-dimensional surface implies an $O(\sqrt[6]{N})$ converge with the number of grid points $N = (L/\Delta a)^2$. We believe that it is this poor scaling why even a world-leading adhesion simulator like Pastewka [33] abstained from making a direct comparison of approach and retraction of an elastomer from a randomly rough tip and instead has resorted to Persson's contact-mechanics theory [30] to rationalize the observed compression/decompression hysteresis.

A common solution to reducing the continuum-corrections during the approach is to simulate adhesion directly only during retraction, which, however, requires a contact shape optimization to be done, in particular, during the formation of the contact. Such an approach is relatively "cheap" for bodies of high symmetry, such as bodies of revolution. However, it would be prohibitively expensive when applied to irregular surface structures. Moreover, modeling adhesive interfaces with discontinuous stress-displacement relations could scarcely be applied to time-dependent problems, such as bulk visco-elastic hysteresis, which can add to adhesive losses.

The findings for flat-on-flat geometries also apply to uneven surfaces, where the adhesive energy hysteresis γ_{hys} scales similarly unfavorably with mesh size for Hertzian and randomly rough contacts as for flat-on-flat geometries. In particular, we found that quite large Tabor parameters of μ_{T} distinctly exceeding ten, are needed to model the approach curve for an adhesive Hertzian indenter, while the retraction curve can be modeled quite accurately with a Tabor parameter as small as $\mu_{\text{T}} = 2$.

In our simulations, the elastomer's surface facing the indenter was displacement controlled, which is difficult to achieve experimentally due to bulk elasticity. However, this mode of operation should be seen as a bonus allowing additional insight into the dynamics of adhesion to be gained. For example, a critical (tensile) stress σ_{c} can be determined at which the elastomer's surface flattens out upon retraction in addition to the maximum tensile stress, or, pull-off stress, which is measured when the retraction is load driven. Moreover, it may be useful to know the tensile stresses in the simulation of adhesive process during detachment processes, since any local grid point in an adhesive simulation is always in between being displacement and load-driven so that knowledge of the tension as a function of separation is often needed even at those separations that would be macroscopically unstable in a load-driven operation.

To prevent this study from acquiring an even more unbearable length than the one it already has, we did not include our (preliminary) results on the adhesion between randomly rough surfaces. However, it may be in place to justify *a posteriori* the use of exponential functions to describe repulsion and attraction by presenting—also as a teaser for future work— a "measured" cohesive-zone law,

which was obtained by simulating a randomly rough surface in contact with an elastomer. The "microscopic" range of interaction used was $\rho = 0.23\, h_{\rm std}$, where $h_{\rm std}$ is the standard deviation of the height. For this relatively long-range interaction, only a small hysteresis was observed. Roughness did not only decrease the adhesion from its "microscopic" but also the range of repulsion were increased by 60% compared to its microscopic value and the range of adhesion by a factor close to 4.

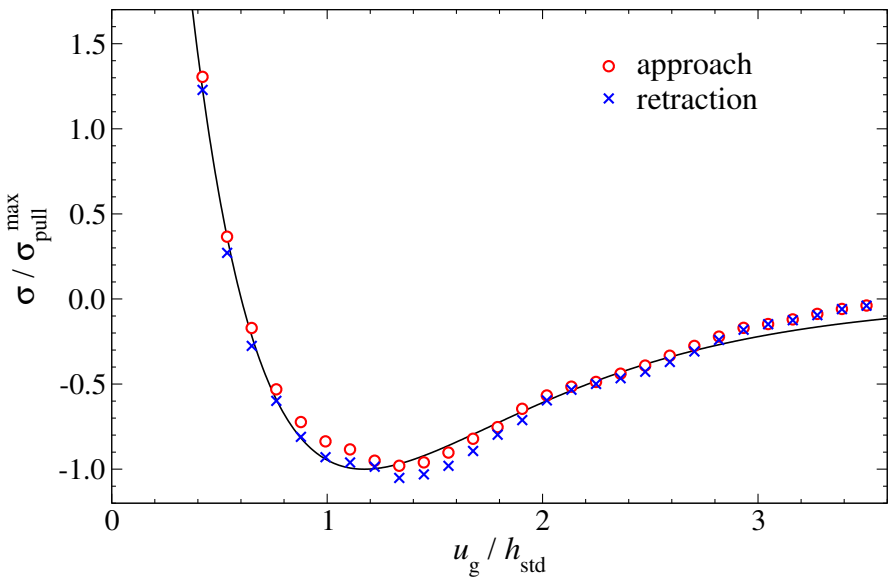

Figure 14. Measured cohesive zone-law resulting from a simulation between, for approach (red circles) and retraction (blue crosses). The full line is a fit to the mean value of the compression and decompression curve, which assumes two exponential functions. Compressive stress is expressed in units of the (fitted) maximum tensile stress, and the mean gap $u_{\rm g}$ is stated in units of the height standard deviation.

This outlook on pull-off forces between randomly rough surfaces suggests that integrating out roughness effects at the small scales reduces not only the adhesion to be used in a cohesive-zone model but also increases the rate of interaction. Both effects combined substantially reduce the stiffness of the contact problem. A true challenge, however, will be to coarse grain the cohesive-zone models so that adhesive hysteresis, including preload effects on the pull-off force, as observed, for example in structured micro pillars [39], can be modeled.

Author Contributions: M.H.M. designed the project. A.W., Y.Z. and M.H.M performed the simulations and analyzed the data. A.W. and M.H.M. wrote the manuscript.

Funding: This research was funded by the German Research Foundation (DFG) through grant number MU 1694/5-2.

Conflicts of Interest: The authors declare no conflict of interest.

Appendix A

The analytical treatments of the defect patterns presented in this section are not fully from first principles, i.e., from using solely the stress-displacement relation introduced later in Eq. (A5). The spatial stress and displacement profiles observed in the simulations for thin and thick ridges, respectively, enter the calculations. Both profiles turn out proportional to $\sqrt{1-(x/a_{\rm c})^2}$. Meaningful approximations to this proportionality yield similar results, i.e., functions that are zero for $|x| > a_{\rm c}$) while symmetric, positive, and continuous otherwise. Numerical constants in the final results change only slightly.

Appendix A.1 Thin-ridge limit

In this section, we derive an expression for the aymptotic $\hat{v}(\alpha \to 1)$ dependence for thin ridges starting from the (known or rather observed) stress profile $\sigma(x)$ in a thin ridge. Towards this end, we calculate the mean gap u_0 from $\sigma(x)$ and then equate $u_0\sigma_0/2$ with the work done by the indenter to deform the elastic body.

The stress in the thin ridge satisfies

$$\sigma(x) = \frac{4\sigma_0}{\pi}\sqrt{1-(x/a_\mathrm{c})^2}\,\Theta(a_\mathrm{c}-x). \tag{A1}$$

For the following calculations, we chose the domain such that $0 < 2x \leq L$ and placed the ridge symmetrically around $x = 0$ so that only the cosine Fourier transform of stress $\tilde{\sigma}_\mathrm{c}(q)$ and displacement fields $\tilde{u}_\mathrm{c}(q)$ are needed. Here $a_c = \bar{\alpha}L/2$ is the half length dimension of thin ridge. The following convention for the Fourier transform is used

$$\sigma(x) = \sum_{n=0,1,\ldots} \tilde{\sigma}_\mathrm{c}\,\cos(q_n\,x) \tag{A2}$$

$$\tilde{\sigma}(q_n) = \frac{2-\delta_{n,0}}{L}\int_{-L/2}^{L/2} dx\,\sigma(x)\,\cos(q\,x) \tag{A3}$$

with $q_n = n/(2\pi L)$. Thus,

$$\tilde{\sigma}_\mathrm{c}(q_n) = 2\,(2-\delta_{n,0})\,\sigma_0\,\frac{J_1(q_n a_\mathrm{c})}{q_n a_\mathrm{c}}. \tag{A4}$$

Using the general relation for the Fourier transforms of stress and displacement,

$$\tilde{\sigma}(q_n) = \frac{q_n\,E^*}{2}\,\tilde{u}(q_n), \tag{A5}$$

which is valid for (frictionless) semi-infinite solids, the mean separation between the two surfaces is obtained as

$$u_0 = \frac{1}{L}\int_{-L/2}^{L/2} dx\,\{u(0)-u(x)\} \tag{A6a}$$

$$= \sum_{n\neq 0}\tilde{u}_\mathrm{c}(q_n) \tag{A6b}$$

$$= \frac{8\,a_\mathrm{c}\,\sigma_0}{E^*}\sum_{n\neq 0}\frac{J_1(q_n a_\mathrm{c})}{(q_n a_\mathrm{c})^2} \tag{A6c}$$

$$\approx \frac{4\sigma_0 L}{\pi E^*}\int_{\pi\bar{\alpha}}^{\infty} dq'\,\frac{J_1(q')}{q'^2} \tag{A6d}$$

$$\approx \frac{4\sigma_0 L}{\pi E^*}\left\{-\frac{\ln(\pi\bar{\alpha})}{2}+c\right\} \quad \text{for } \pi\bar{\alpha} \ll 1, \tag{A6e}$$

where the constant c was deduced numerically to be $c \approx 0.30797$. In Eq. (A6), $J_1(x)$ denotes a Bessel function of the first kind, for which $J_1(x) \approx x/2$ when $x \ll 1$. This approximation proves useful to determine the prefactor of the $\ln(\pi\bar{\alpha})$ term. Moreover, the $\sum_n f(q_n)$ was approximated with an integral $\frac{L}{2\pi}\int_0^\infty dq\,f(q)$.

Eq. (A6e) can be solved for σ_0 so that using $v_\mathrm{ela} = u_0\,\sigma_0/2$

$$v_\mathrm{ela} = \frac{\pi}{-4\ln(\pi\bar{\alpha})+8c}\,\frac{E^* u_0^2}{L} \tag{A7}$$

is obtained.

Appendix A.2 Thick-ridge limit

For the thick-ridge limit, we proceed similarly as for the thin-ridge limit. However, we now chose the center-of-mass of the non-contact pattern to coincide with $x = 0$ and define $\bar{a}_c$ as half of the non-contact width. Moreover, we now observe the displacement to satisfy

$$u(x) = \frac{4u_0}{\pi}\sqrt{1-(x/\bar{a}_c)^2}\,\Theta(\bar{a}_c - x). \tag{A8}$$

Using the cosine Fourier transform, the results for the stress obtained in Sect. A.1 can be used again so that

$$\tilde{u}_c(q_n) = 2\,(2-\delta_{n,0})\,u_0\,\frac{J_1(q_n a_c)}{q_n a_c}. \tag{A9}$$

Thus, the elastic energy stored in the defect pattern is

$$\begin{aligned} v_{\text{ela}} &= \frac{E^*}{4}\sum_{n=1,2,\ldots} q_n\,\tilde{u}_c^2(q_n) && \text{(A10a)}\\ &= 4E^* u_0^2 \sum_{n=1,2,\ldots}\frac{J_1^2(q_n a_c)}{q_n a_c^2} && \text{(A10b)}\\ &\approx \frac{2\,E^* u_0^2\,L}{\pi\,a_c^2}\int dq'\,\frac{J_1^2(q')}{q'} && \text{(A10c)}\\ &= \frac{E^* u_0^2\,L}{2\,\pi\,a_c^2} && \text{(A10d)} \end{aligned}$$

Since $a_c = (1-\alpha)\,L/2$, it follows that

$$\hat{v}_{\text{ela}} = \frac{2}{\pi(1-\alpha)^2}. \tag{A11}$$

References

1. Persson, B.N.; Albohr, O.; Tartaglino, U.; Volokitin, A.; Tosatti, E. On the nature of surface roughness with application to contact mechanics, sealing, rubber friction and adhesion. *Journal of Physics: Condensed Matter* **2004**, *17*, R1.
2. Fischer, S.C.; Arzt, E.; Hensel, R. Composite pillars with a tunable interface for adhesion to rough substrates. *ACS Applied Materials & Interfaces* **2017**, *9*, 1036–1044.
3. Dugdale, D.S. Yielding of steel sheets containing slits. *Journal of the Mechanics and Physics of Solids* **1960**, *8*, 100–104.
4. Needleman, A. A Continuum Model for Void Nucleation by Inclusion Debonding. *Journal of Applied Mechanics* **1987**, *54*.
5. Park, K.; Paulino, G.H. Cohesive zone models: a critical review of traction-separation relationships across fracture surfaces. *Applied Mechanics Reviews* **2011**, *64*.
6. Hutchinson, J.; Evans, A. Mechanics of materials: top-down approaches to fracture. *Acta Materialia* **2000**, *48*, 125–135.
7. Müser, M.H. Single-asperity contact mechanics with positive and negative work of adhesion: influence of finite-range interactions and a continuum description for the squeeze-out of wetting fluids. *Beilstein Journal of Nanotechnology* **2014**, *5*, 419–437.
8. Li, Q.; Kim, K.S. Micromechanics of rough surface adhesion: a homogenized projection method. *Acta Mechanica Solida Sinica* **2009**, *22*, 377–390.
9. Yao, H.; Gao, H. Mechanics of robust and releasable adhesion in biology: Bottom–up designed hierarchical structures of gecko. *Journal of the Mechanics and Physics of Solids* **2006**, *54*, 1120–1146.

10. Alfano, G.; Crisfield, M. Finite element interface models for the delamination analysis of laminated composites: mechanical and computational issues. *International Journal for Numerical Methods in Engineering* **2001**, *50*, 1701–1736.
11. Samimi, M.; Van Dommelen, J.; Geers, M. An enriched cohesive zone model for delamination in brittle interfaces. *International Journal for Numerical Methods in Engineering* **2009**, *80*, 609–630.
12. Hillerborg, A.; Modéer, M.; Petersson, P.E. Analysis of crack formation and crack growth in concrete by means of fracture mechanics and finite elements. *Cement and Concrete Research* **1976**, *6*, 773–781.
13. Irwin, G. Plastic zone near a crack and fracture toughness. *Proceedings of the seventh Sagamore Ordnance material conference* **1997**, *4*, 63–78.
14. Falk, M.L.; Needleman, A.; Rice, J.R. A critical evaluation of cohesive zone models of dynamic fractur. *Le Journal de Physique IV* **2001**, *11*, Pr5–43.
15. Hui, C.Y.; Bennison, S.; Londono, J. Crack blunting and the strength of soft elastic solids. *Proceedings of the Royal Society of London. Series A: Mathematical, Physical and Engineering Sciences* **2003**, *459*, 1489–1516.
16. Pohrt, R.; Popov, V.L. Adhesive contact simulation of elastic solids using local mesh-dependent detachment criterion in boundary elements method. *Facta Universitatis, Series: Mechanical Engineering* **2015**, *13*, 3–10.
17. Popov, V.L.; Pohrt, R.; Li, Q. Strength of adhesive contacts: Influence of contact geometry and material gradients. *Friction* **2017**, *5*, 308–325.
18. Johnson, K.L.; Kendall, K.; Roberts, a. Surface energy and the contact of elastic solids. *Proceedings of the royal society of London. A. mathematical and physical sciences* **1971**, *324*, 301–313.
19. Alfano, G. On the influence of the shape of the interface law on the application of cohesive-zone models. *Composites Science and Technology* **2006**, *66*, 723–730.
20. Volokh, K.Y. Comparison between cohesive zone models. *Communications in Numerical Methods in Engineering* **2004**, *20*, 845–856.
21. Mie, G. Zur kinetischen Theorie der einatomigen Körper. *Annalen der Physik* **1903**, *316*, 657–697.
22. Jones, J.E. On the determination of molecular fields.—II. From the equation of state of a gas. *Proceedings of the Royal Society of London. Series A, Containing Papers of a Mathematical and Physical Character* **1924**, *106*, 463–477.
23. Israelachvili, J.N. *Intermolecular and surface forces*; Academic press, 2011.
24. Persson, B.N.J. Relation between Interfacial Separation and Load: A General Theory of Contact Mechanics. *Physical Review Letters* **2007**, *99*, 125502. doi:10.1103/physrevlett.99.125502.
25. Almqvist, A.; Campañá, C.; Prodanov, N.; Persson, B.N.J. Interfacial separation between elastic solids with randomly rough surfaces: Comparison between theory and numerical techniques. *Journal of the Mechanics and Physics of Solids* **2011**, *59*, 2355–2369. doi:10.1016/j.jmps.2011.08.004.
26. Campaná, C.; Müser, M.H. Practical Green's function approach to the simulation of elastic semi-infinite solids. *Physical Review B* **2006**, *74*, 075420.
27. Zhou, Y.; Moseler, M.; Müser, M.H. Solution of boundary-element problems using the fast-inertial-relaxation-engine method. *Physical Review B* **2019**, *99*, 144103.
28. Müser, M.H.; Zhou, Y.; Wang, A. How thermal fluctuations affect hard-wall repulsion and thereby Hertzian contact mechanics. *Frontiers in Mechanical Engineering* **2019**, *5*, 67.
29. Tomlinson, G. CVI. A molecular theory of friction. *The London, Edinburgh, and Dublin philosophical magazine and journal of science* **1929**, *7*, 905–939.
30. Persson, B. Adhesion between an elastic body and a randomly rough hard surface. *The European Physical Journal E* **2002**, *8*, 385–401.
31. Pastewka, L.; Robbins, M.O. Contact between rough surfaces and a criterion for macroscopic adhesion. *Proceedings of the National Academy of Sciences* **2014**, *111*, 3298–3303.
32. Müser, M.H.; Dapp, W.B.; Bugnicourt, R.; Sainsot, P.; Lesaffre, N.; Lubrecht, T.A.; Persson, B.N.; Harris, K.; Bennett, A.; Schulze, K.; others. Meeting the contact-mechanics challenge. *Tribology Letters* **2017**, *65*, 118.
33. Dalvi, S.; Gujrati, A.; Khanal, S.R.; Pastewka, L.; Dhinojwala, A.; Jacobs, T.D.B. Linking energy loss in soft adhesion to surface roughness. *Proceedings of the National Academy of Sciences* **2019**, *116*, 25484–25490. doi:10.1073/pnas.1913126116.
34. Shenoy, V.; Sharma, A. Pattern formation in a thin solid film with interactions. *Physical Review Letters* **2001**, *86*, 119.

35. Shenoy, V.; Sharma, A. Stability of a thin elastic film interacting with a contactor. *Journal of the Mechanics and Physics of Solids* **2002**, *50*, 1155–1173.
36. Griffith, A.A. VI. The phenomena of rupture and flow in solids. *Philosophical transactions of the royal society of london. Series A* **1921**, *221*, 163–198.
37. Maugis, D.; Barquins, M. Fracture mechanics and the adherence of viscoelastic bodies. *Journal of Physics D: Applied Physics* **1978**, *11*, 1989–2023. doi:10.1088/0022-3727/11/14/011.
38. Guduru, P. Detachment of a rigid solid from an elastic wavy surface: theory. *Journal of the Mechanics and Physics of Solids* **2007**, *55*, 445–472.
39. Noderer, W.; Shen, L.; Vajpayee, S.; Glassmaker, N.; Jagota, A.; Hui, C.Y. Enhanced adhesion and compliance of film-terminated fibrillar surfaces. *Proceedings of the Royal Society A: Mathematical, Physical and Engineering Sciences* **2007**, *463*, 2631–2654.
40. Müser, M.H.; Urbakh, M.; Robbins, M.O. Statistical mechanics of static and low-velocity kinetic friction. *Advances in Chemical Physics* **2003**, p. 187.
41. Allen, M.P.; Tildesley, D.J. *Computer Simulations of Liquids*; Oxford University Press: Oxford, 2017.
42. Müser, M.H. A dimensionless measure for adhesion and effects of the range of adhesion in contacts of nominally flat surfaces. *Tribology International* **2016**, *100*, 41–47.
43. Turon, A.; Davila, C.G.; Camanho, P.P.; Costa, J. An engineering solution for mesh size effects in the simulation of delamination using cohesive zone models. *Engineering Fracture Mechanics* **2007**, *74*, 1665–1682.